Science Advances
AAAS

Supplementary Materials for

Solution-shearing of dielectric polymer with high thermal conductivity and electric insulation

Zheng Li, Lu An, Saurabh Khuje, Jingye Tan, Yong Hu, Yulong Huang, Donald Petit, Danial Faghihi, Jian Yu, Shenqiang Ren*

*Corresponding author. Email: shenren@buffalo.edu

Published 29 September 2021, *Sci. Adv.* **7**, eabi7410 (2021)
DOI: 10.1126/sciadv.abi7410

This PDF file includes:

Supplementary Text

Crystallinity and plane distances calculation based on XRD technique

Based on the X-ray diffraction (XRD) spectra of SUPE films at different shearing speeds, there are two distinct diffraction peaks at 21.44° and 23.99°, corresponding to the (110) and (200) crystal plane of SUPE films. Due to residue shear stress induced by solution shearing process in the SUPE films, there are D-spacing shifts of the (200) plane and (110) plane observed in the XRD spectra. The plane distance (D-spacing) of these two crystal planes is changed as a result of the residue shear stress. The D-spacing could be calculated by Bragg's equation below,

$$d_{(hkl)} = \frac{\lambda}{2\sin(\theta)}$$

.

The polymer chain alignment could be enhanced by solution shearing process, which cause a high crystallinity. The crystallinity of solution sheared SUPE films could be calculated by the area ratios between the sharp crystalline peaks and the broad, amorphous peak.

There exists an average dielectric constant (4.45 for SUPE/BN composite with 4 wt% BN) as increasing the BN concentration, compared with the average dielectric constant of 4.17 for pure SUPE under the frequency of 10^3 Hz. The DFs of all materials show the lowest value under the frequency of 3×10^3 Hz, e.g., 0.0013 for SUPE/BN composite with 4 wt% BN loading. As the frequency increases from 10^3 to 10^6 Hz, the DF of SUPE/BN composite with 4 wt% BN is changed less than 0.001, indicating the stable and low DF values for various frequencies. Here, SUPE/BN(1) indicates 1 wt% BN loading into the SUPE matrix. With the BN concentrations increasing from 1 wt% to 6 wt%, the yield strengths increase from 8.5 MPa to 17.5 MPa, which is caused by the reinforcement of BN nanosheets.

The initial thermal decomposition of SUPE/BN is 429℃, lower than that of SUPE of 436℃. After the complete decomposition, the composite's residue is higher than pure SUPE film due to BN nanosheet fillers. Here, SUPE/BN(1) indicates the BN concentrations of 1 wt%. The existences of BN and SUPE are verified by XRD technique. The two distinct peaks at 21.44° and 23.99° are corresponding to the (110) and (200) crystal plane of SUPE. A peak around 36° is (020) crystal plane of SUPE. The (002) crystal plane of BN is around 26°. With increasing BN concentrations, the $(002)_{BN}$ peak intensity would increase, which is consistent with the higher concentrations of BN. Here, SUPE/BN(1) indicates the composite with 1 wt% BN. Here, SUPE/BN(1) indicates the composite with 1 wt% BN. For Raman mapping, with BN concentration increases, the peak intensity around the wavelength of 1300 cm^{-1} is increasing. Pure SUPE shows the best transmittance performance with 65% around NIR region and 40% around visible region. As increasing BN concentrations, the SUPE/BN composites show the decreased transmittance from the near infrared (NIR) region to the visible region due to the increased scattering effect. The more BN is added, the less light is transmitted through the SUPE/BN composites. When the BN concentration is larger than 2 wt%, the light transmittance is largely blocked with an increased opaque performance.

The dimensions of BN nanosheets show the triangle shape stacked together, so the multiple sets of diffraction patterns are demonstrated. After incorporation of BN nanosheets in SUPE, the transparency decreases showing the semi-transparency performance.

Mechanical, electrical and thermal measurements

Tensile stress-strain curves for the sheared SUPE or UHMWPE/BN samples with dog-bone-like mold are performed with a Mark-10 universal testing machine. The load resolution speed was 0.5 N and 13 mm/min respectively, and AF009 indicator accurately recorded the travel distance. The tensile test was stopped until the sample was broken.

Breakdown test following ASTM D-149-97a standards is carried out by placing sample between the top electrode connected to a high-voltage supply and the bottom electrode connected to the ground. The applied voltage was increased from zero with 500 V/s rate until breakdown occurred

and the thickness of the specimen was tested using a micrometer. The electrical measurements were carried out using Keithley 2450 SourceMeter.

The thermal conductivities of SUPE films were carried out by using Hot Disk TPS-2200 according to the ISO standard 22007-2, while the double-sided samples (50 mm length × 50 mm width × ~ 200 μm thickness) were placed on the 7854 (radius 10.5 mm, thin film measurements) and 5465 Kapton sensor (radius 3.2 mm, anisotropic measurement) for the measurements. The TPS sensor acts both as a heat source to increase the temperature of the sample and also as a "resistance thermometer" for monitoring the temperature increase versus time with extremely precision during the measurement. During the measurement, 1-kg brass weight was applied to the entire system to ensure a good contact of the sensor with the SUPE film surface and a protective cover is put over the assembly. After a series of experimental testing, we select 200 mW of heating power over a duration of 10 s. In the process of selection of time interval, these testing parameters are optimized such that the suitable total temperature rise is between 2 K and 5 K. The thermal penetration depths of all the measurements are confirmed to be smaller than any of the SUPE film sample dimensions. The temperature-dependent time was recorded, and the time interval was selected for analyzing and calculating the thermal conductivity along the out-of-plane and in-plane directions by using the anisotropic testing module. For each sample, we performed 5 repeated measurements with the waiting time between each measurement of 30 min, sufficient for the system to cool back to room temperature.

The transient heat transfer method is applied to measure in-plane thermal properties. When a certain amount of power is applied for a set amount of time, the sensor can detect temperature change over the course of the allotted time and determine thermal conductivity of sample based on the collected data. Thermal conductivity reported in this study are measured over 5 samples to get an average performance value, while each sample is repeated 5 times to derive the average value reported. To get the anisotropic data of the sample the specific heat per unit volume is obtained for the sample. This is obtained by first finding the specific heat per unit mass of UHMWPE, and then converting to volumetric specific heat by using the density of UHMWPE. The following equations are used to obtain the anisotropic thermal conductivity.

$$\Delta T = \frac{P}{r \cdot \sqrt{k_a k_r} \cdot \pi^{\frac{3}{2}}} \cdot D(\tau_r) \quad (1)$$

$$\tau_r = \sqrt{\frac{t}{\theta_r}} \quad (2)$$

$$\theta_r = \frac{r^2}{\alpha_r} \quad (3)$$

Where: Δ T is the temperature different of TPS sensor; P is the output of power from the sensor; r is the radius of the sensor's heating source; K_a and K_r are the thermal conductivity in the axial and radial direction; $D(\tau_r)$ is the time measured from the start of the transient recording; θ_r is the characteristic time; α_r is the thermal diffusivity of the sample in the axial direction.

Error in the TPS measurement can potentially come from two sources: (1) uncertainty in the experimental data and the selection of time interval for analysis, and (2) deviation of the original idealized analytical heat transfer model from the practical measurement scenario. We chose the appropriate time interval to calculate thermal conductivity and simultaneously make sure all other paraments (BG thermal conductivity, BG thermal diffusivity, BG specific heat, probing depth, temperature increase, temperature drift, total to characteristic time, total temperature increase, time correction, mean deviation, and sensor resistance) within a range. The standard Kapton® polyimide thin films and NIST-standard polystyrene polymer reference material (with certificate) have been applied as the control sample to verify the accuracy of TPS-2200 instrument. All standard samples have been confirmed by using the steady-state measurements to verify its thermal conductivity from

the certified values. Furthermore, we cross-checked one of our polyethylene films using the FDTR technique which suggests high thermal conductivity along polymer chain aligned direction. The thermal conductivity results obtained in this work agree well with other measurement techniques and international standard polymeric materials. This agreement indicates that the TPS method we applied in this work is accurate to within the error bar (within ±5%) over a thermal conductivity range. In addition, Fig. S7 shows the time-temperature trace for the SUPE sample with the shearing speed of 10 mm/s. The measurement parameters include the heat power of 200 mW, the measurement time of 10 s, and the specific heat capacity of 1.83 MJ/m^{3}K.

Finite element simulations of the steady-state temperature distribution

In both simulations, the bottom surface is fixed to the temperature of 200 ^{o}C, and the body is exposed to convection with the ambient. Due to the much higher conductivity of UHMWPE in the x-direction, the lower temperature distribution is obtained compared to Kapton. The average internal temperature in aligned UHMWPE is 52.5 ^{o}C and in Kapton is 89.9 ^{o}C.

The heat transfer model used for simulating the steady-state temperature distribution $T(\boldsymbol{x})$ in materials governed by the following partial differential equation,

$$\nabla \cdot \left(\boldsymbol{K}\nabla T(\boldsymbol{x})\right) = 0 \quad (4)$$

where $\boldsymbol{K}$ is the general conductivity tensor,

$$\boldsymbol{K} = \begin{bmatrix} K_{xx} & K_{xy} & K_{xz} \\ K_{yx} & K_{yy} & K_{yz} \\ K_{zx} & K_{zy} & K_{zz} \end{bmatrix} \quad (5)$$

For the simulations presented in this paper, we considered orthotropic materials such that $K_{xy} = K_{yx} = K_{xz} = K_{zx} = K_{zy} = K_{yz} = 0$. We assumed Kapton is an isotropic material and assigned $0.17\ \mathrm{W\,m^{-1}\,K^{-1}}$ to the all the diagonal components of the conductivity tensor. For the aligned UHMWPE, we considered $K_{yy} = K_{zz} = 0.17\ \mathrm{W\,m^{-1}\,K^{-1}}$ and $K_{xx} = 11\ \mathrm{W\,m^{-1}\,K^{-1}}$. The convection boundary condition has the following form,

$$(\boldsymbol{K}\nabla T) \cdot \boldsymbol{n} = h(T - T_{amb}) \quad (6)$$

where $T_{amb} = 0$ ^{o}C is the ambient temperature, $\boldsymbol{n}$ is the normal vector to the surface of the domain, and $h = 50\ \mathrm{MW\,m^{-2}\,K^{-1}}$ is convective heat transfer coefficient. The governing equation, along with the boundary conditions, are solved by the finite element method using the commercial software ABAQUS. For the simulation results presented in Fig. 3E-F, a domain 800 microns x 800 microns x 150 microns is taken into account and discretized by 20 elements in each direction.

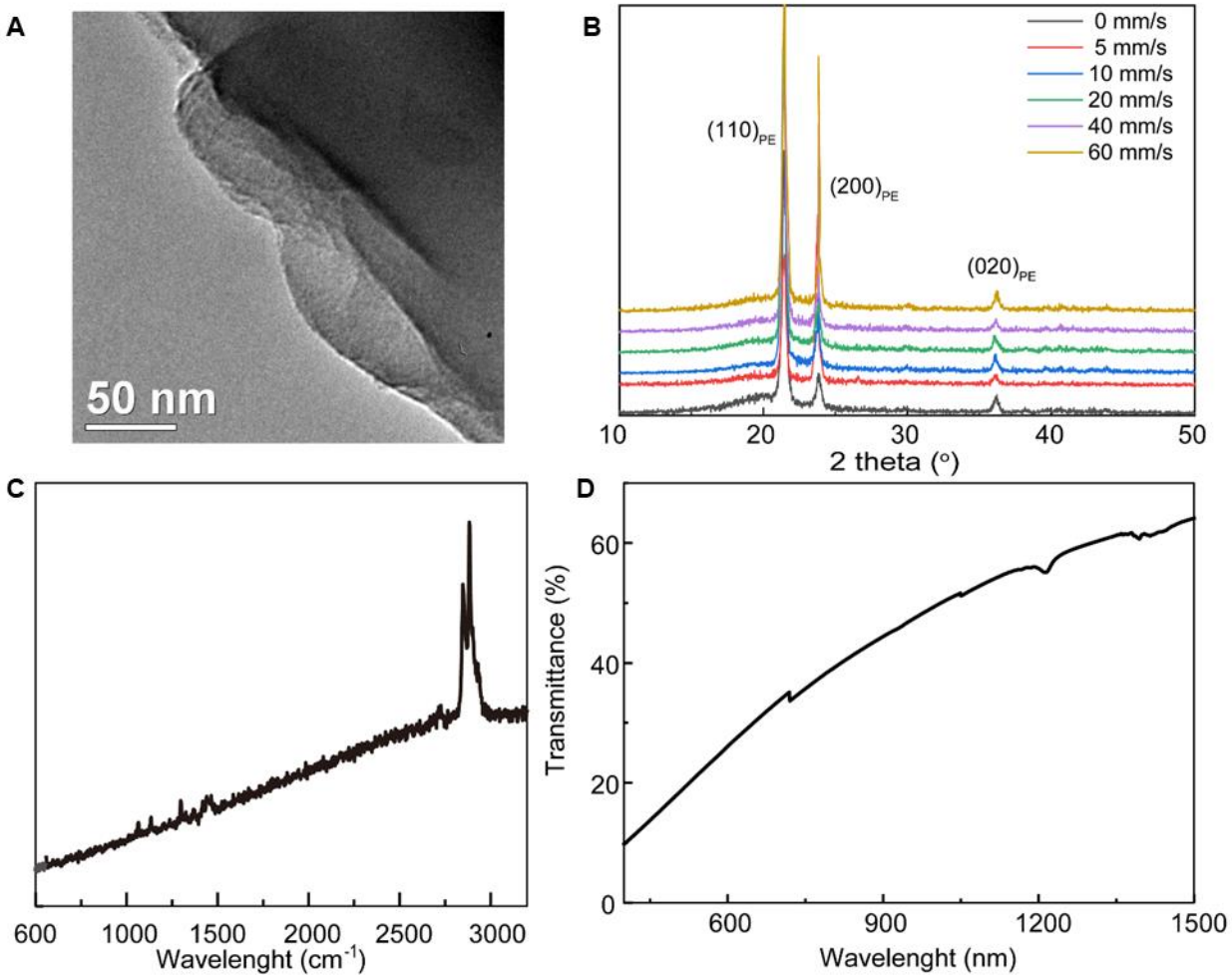

Fig. S1. Morphological and structural characterization of SUPE. (**A**) Transmission electron microscopes (TEM) for SUPE thin film. (**B**) X-ray diffraction (XRD) patterns of SUPE with different shearing speed. (**C**) Raman spectra of SUPE. (**D**) UV-Vis transmittance spectra of SUPE.

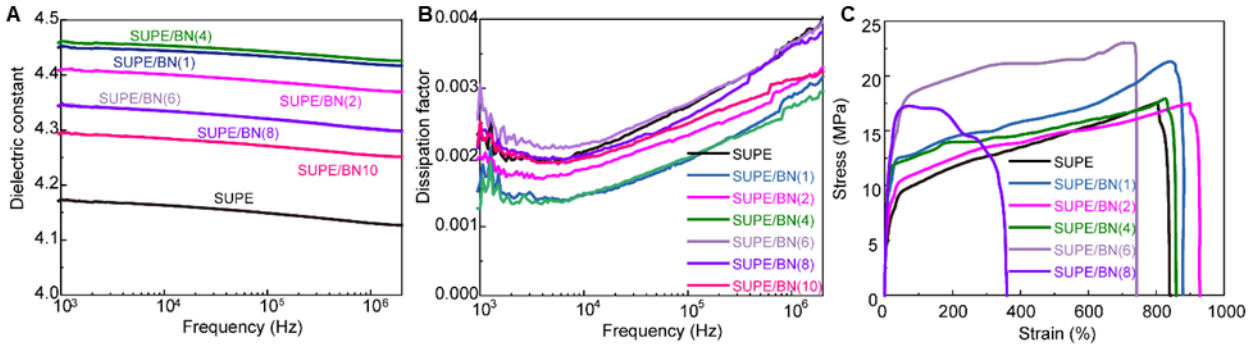

Fig. S2. Dielectric and mechanical performance of SUPE and SUPE/BN composites. Frequency dependence of (**A**) Dielectric constant, and (**B**) Dissipation factor (DF) of pure UHMWPE (SUPE), and UHMWPE/BN (SUPE/BN) with different BN concentrations. (**C**) Tensile stress vs. strain curves of SUPE and SUPE/BN composites with different concentrations of BN.

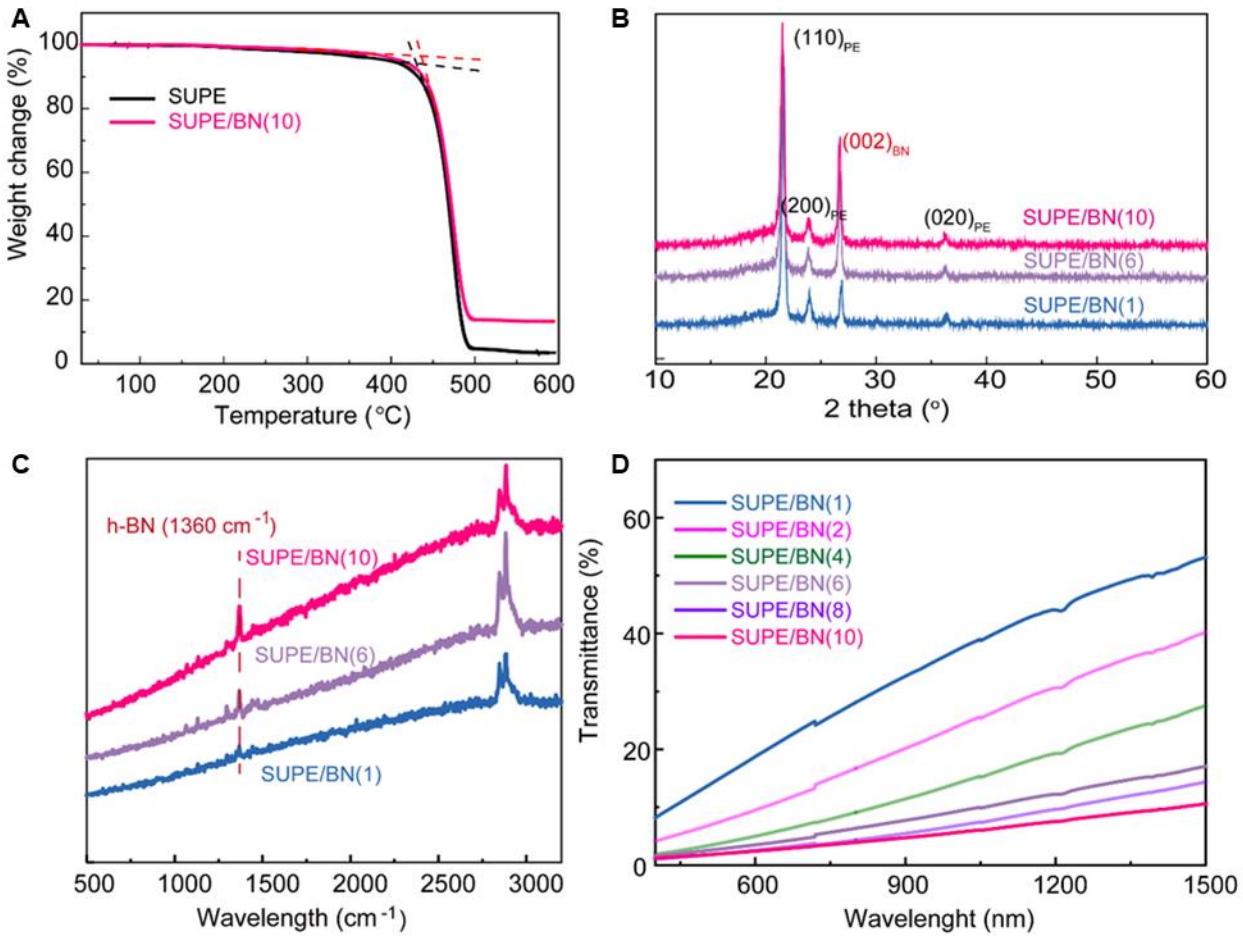

Fig. S3. Structural properties of SUPE and SUPE/BN composites. (**A**) Thermogravimetric analysis (TGA) for SUPE film, and SUPE/BN composite film. (**B**) X-ray diffraction (XRD) patterns of SUPE/BN with different BN concentrations. (**C**) Raman spectra of SUPE/BN with different BN concentrations. (**D**) UV-Vis transmittance spectra of SUPE/BN with different BN concentrations.

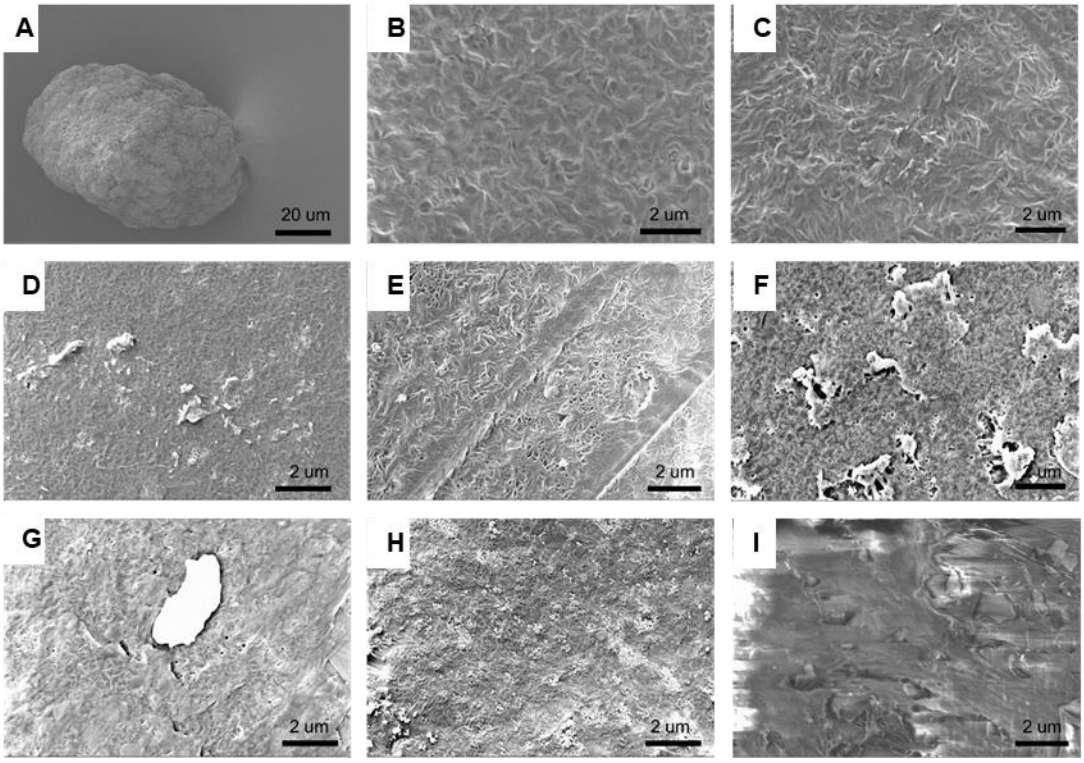

Fig. S4. SEM images of UHMWPE and UHMWPE/BN composites. (**A**) SEM images of pure UHMWPE feedstock powders. (**B**) The magnified SEM image of UHMWPE. The disordered fibrous morphology could be observed before solution gel shearing treatment. SEM images of UHMWPE/BN with BN concentrations of (**C**) 1, (**D**) 2, (**E**) 4, (**F**) 6, (**G**) 8, (**H**) 10 wt%. With increasing BN concentrations, the more BN nanosheets are found in SEM images. (**I**) Cross-section SEM images of SUPE/BN(4), where the BN nanosheets are inserted into SUPE matrix.

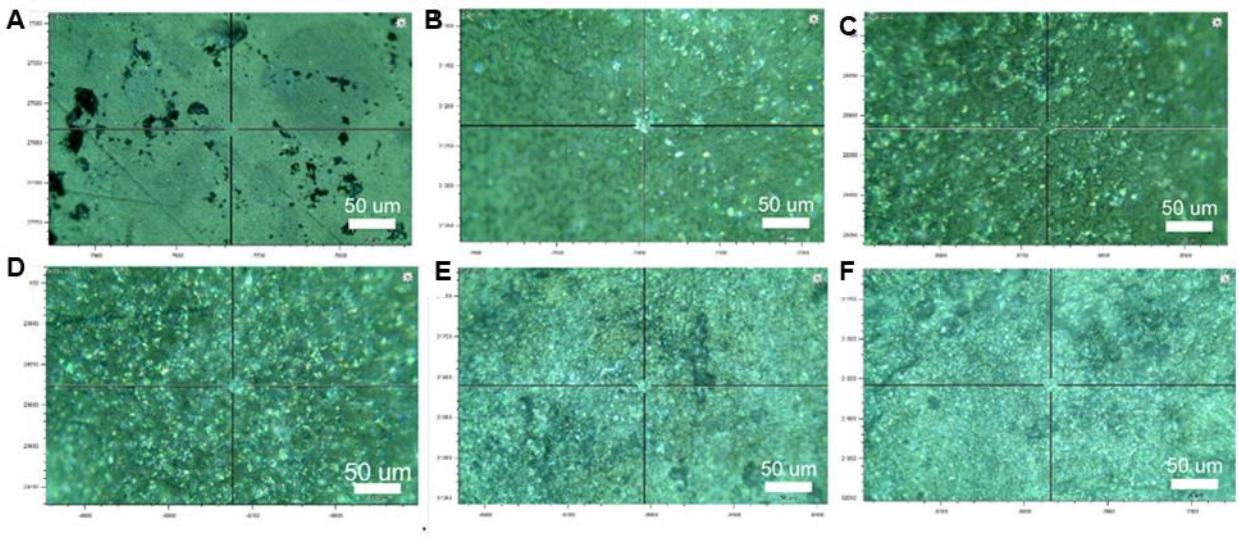

Fig. S5. Optical images of SUPE and SUPE/BN composites for Raman mapping. Optical images of (**A**) SUPE, (**B**) SUPE/BN(1), (**C**) SUPE/BN(2), (**D**) SUPE/BN(4), (**E**) SUPE/BN(6), (**F**) SUPE/BN(8) for Raman mapping. Here, SUPE/BN(1) indicates the composite with 1 wt% BN. The distributions of BN nanosheets in the optical images show the increasement tendency with increasing the BN concentrations.

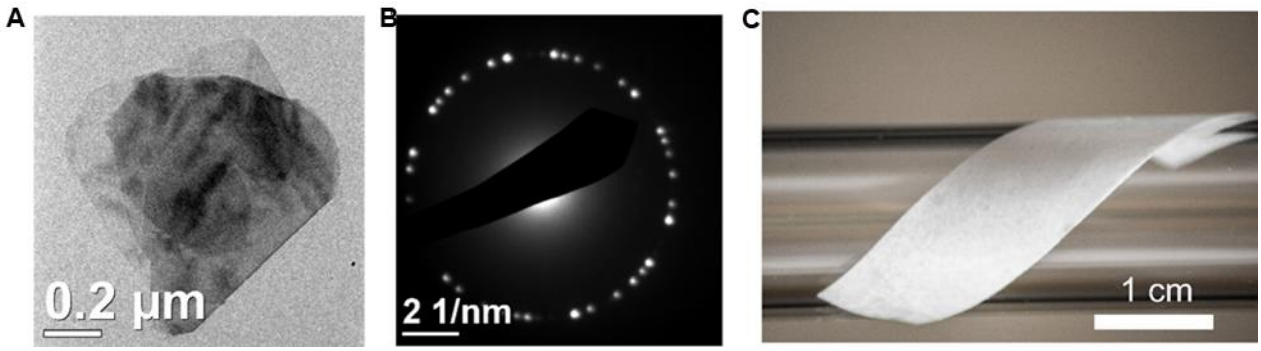

Fig. S6. TEM images of BN and picture of UHMWPE/BN composite. (**A**) TEM image of BN flakes. (**B**) The TEM diffraction pattern of BN flakes. (**C**) UHMWPE/BN composite.

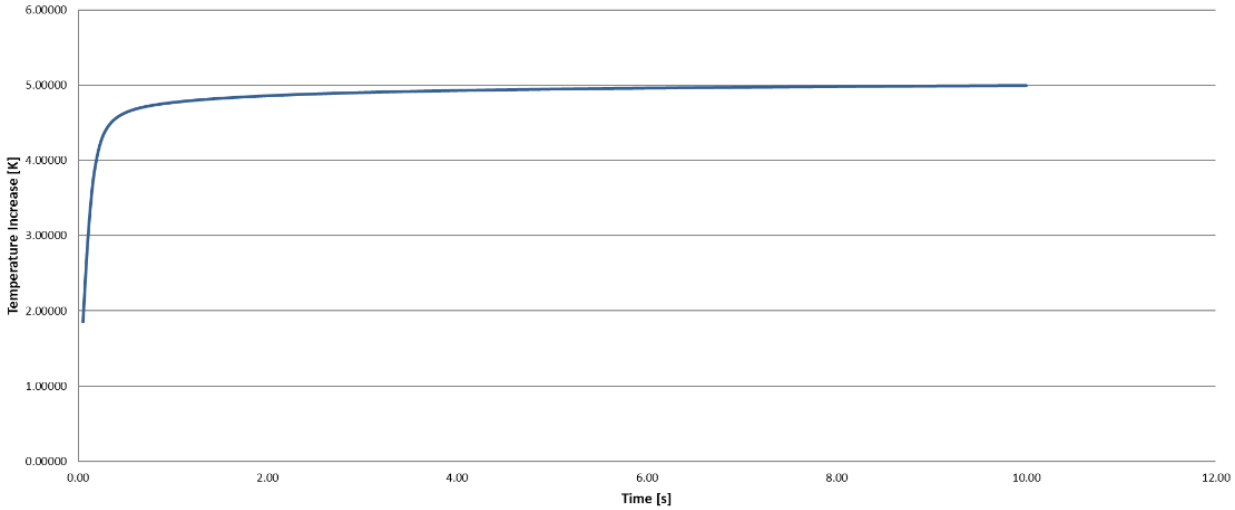

Fig. S7. Time-temperature trace for the SUPE sample with shearing speed of 10 mm/s.